Geochemistry Geophysics Geosystems G3
AN ELECTRONIC JOURNAL OF THE EARTH SCIENCES
Published by AGU and the Geochemical Society

Article
Volume 10, Number 10
14 October 2009
Q10Y06, doi:10.1029/2009GC002750
ISSN: 1525-2027

Magnetic field microscopy of rock samples using a giant magnetoresistance–based scanning magnetometer

Fatim Hankard
Department of Geophysics and Planetology, CEREGE, Aix-Marseille University, CNRS, BP80, F-13545 Aix-en-Provence CEDEX 4, France

Now at Department of Geological Sciences, University of Michigan, C.C. Little Building, 1100 North University Avenue, Ann Arbor, Michigan 48109-1005, USA (hankard@umich.edu)

Jérôme Gattacceca
Department of Geophysics and Planetology, CEREGE, Aix-Marseille University, CNRS, BP80, F-13545 Aix-en-Provence CEDEX 4, France

Claude Fermon and Myriam Pannetier-Lecoeur
SPEC, IRAMIS, DSM, CEA Saclay, F-91191 Gif-sur-Yvette CEDEX, France

Benoit Langlais
Laboratoire de Planétologie et Géodynamique de Nantes, UMR 6112, Université de Nantes, CNRS, F-44322 Nantes, France

Yoann Quesnel and Pierre Rochette
Department of Geophysics and Planetology, CEREGE, Aix-Marseille University, CNRS, BP80, F-13545 Aix-en-Provence CEDEX 4, France

Suzanne A. McEnroe
Geological Survey of Norway, Trondheim N-7491, Norway

[1] We have developed a new scanning magnetic microscope to image with micrometric resolution magnetic fields originating from room temperature polished samples. This microscope is based on a giant magnetoresistance (GMR) sensor working at room temperature. These magnetic sensors are sensitive to the in-plane components of the magnetic field. The size of the sensing element is 9 μm $\times$ 36 μm. The noise of the GMR sensor is dominated by a low-frequency 1/f noise. The field equivalent noise of the sensors is 10 $nT/\sqrt{Hz}$ at 1Hz and decreases to 0.3 $nT/\sqrt{Hz}$ above 1 kHz for a 1 mA sensing current. The spatial resolution of the system is $\sim$20 μm, and its peak-to-peak noise during operation is $\sim$250 nT. Its high spatial resolution and a minimum sensor-to-sample distance of 30 μm compensate for its rather moderate field sensitivity. This room temperature small-sized and rugged magnetic microscope appears as a powerful instrument for small-scale rock magnetic investigations.

Components: 5185 words, 6 figures.

Keywords: geomagnetism; paleomagnetism; magnetic fields and magnetism; magnetic anomalies; rock and mineral magnetism; instruments and techniques.

Index Terms: 6030 Planetary Sciences: Comets and Small Bodies: Magnetic fields and magnetism; 1517 Geomagnetism and Paleomagnetism: Magnetic anomalies: modeling and interpretation; 0594 Computational Geophysics: Instruments and techniques.

Received 20 July 2009; **Revised** 19 August 2009; **Accepted** 28 August 2009; **Published** 14 October 2009.

Hankard, F., J. Gattacceca, C. Fermon, M. Pannetier-Lecoeur, B. Langlais, Y. Quesnel, P. Rochette, and S. A. McEnroe (2009), Magnetic field microscopy of rock samples using a giant magnetoresistance–based scanning magnetometer, *Geochem. Geophys. Geosyst.*, *10*, Q10Y06, doi:10.1029/2009GC002750.

Theme: Advances in Instrumentation for Paleomagnetism and Rock Magnetism
Guest Editors: M. Fuller, B. Goodman, J. Kirschvink, and K. Verosub

1. Introduction

[2] In the last decade, investigations of small-scale magnetic properties of terrestrial and extraterrestrial rocks have benefited from the development of high-resolution and high-sensitivity magnetic scanning devices devoted to Earth Sciences. This broke through, in particular, with the emergence of a number of scanning Superconducting Quantum Interference Device (SQUID) microscopes [*Thomas and Moyer*, 1992; *Nowaczyk et al.*, 1998; *Egli and Heller*, 2000; *Baudenbacher et al.*, 2002, 2003; *Wang et al.*, 2003; *Fong et al.*, 2005].

[3] Magnetic scanning techniques based on high–transition temperature (high-Tc) SQUID sensors have emerged about ten years ago in the field of Earth Sciences [*Nowaczyk et al.*, 1998; *Egli and Heller*, 2000] with sensors that are cooled down to the boiling temperature of liquid nitrogen (77 K). This magnetic mapping technique is faced with problems related to the cooling system and the temperature difference between the sensor and the sample held at room temperature. These problems make the experiments somewhat delicate. Moreover, spatial resolution of these instruments was never better than ~1 mm. Consequently, these high-Tc SQUID scanning magnetometers have never really been successfully applied to rock magnetism or paleomagnetism studies besides the pilot study in which they are described.

[4] At present, the most powerful of these instruments is the low–transition temperature (low-Tc) SQUID microscope [*Baudenbacher et al.*, 2002, 2003; *Fong et al.*, 2005]. This instrument is able to map the vertical component of the magnetic field above polished slices and thin sections with a spatial resolution of ~100 μm and a subnanotesla field sensitivity. However, this high-performance low-Tc SQUID microscope requires very specific technological skills since the sensor is cooled down at 4 K and brought into a very close proximity, ~100 μm at best, to the sample that is held at room temperature. This is a challenging task as the 4 K SQUID sensor is only separated from the room temperature medium by a 35-μm-thick sapphire window, making therefore the experiments somewhat difficult and costly. In spite of this limitation, these instruments have produced a significant amount of scientific results in the field of Earth and planetary sciences [*Weiss et al.*, 2000; *Gattacceca et al.*, 2006; *Weiss et al.*, 2007a, 2007b, 2008].

[5] On one hand, SQUID-based instruments have now achieved impressive field sensitivity and can detect magnetized particles with moment $\sim 10^{-15}$ Am^2 (i.e., 10^3 better than conventional SQUID magnetometer) but on the other hand, they are now very close to their ultimate achievable spatial resolution both because of the sensor diameter and sensor-to-sample distance.

[6] In order to circumvent problems that mostly emanate from the elevated cost and technical complexity of the cooling systems, new generations of room temperature scanning magnetic field techniques have been recently developed.

[7] A room temperature scanning magnetic microscope based on an amorphous wire magnetoimpedance (MI) sensor was proposed by *Uehara and Nakamura* [2007, 2008]. This scanning MI microscope maps the vertical (i.e., perpendicular to sample plane) component of the magnetic field, as do the SQUID-based microscopes. This instrument achieves a spatial resolution of 400 μm and a field sensitivity of 10 nT. However, to be operational, the MI sensor requires application of a constant bias field of ~50 μT, which induces a magnetic field in the sample. Moreover, the 5.5-mm-long wire length integrates the field over its length. Consequently, these problems tend to blur the magnetic images, and prevent from getting a spatial resolution better than half a millimeter.

[8] Recently, *Kletetschka and Adachi* [2008] have developed a Hall effect–based scanning magnetic field device that also provides maps of the vertical

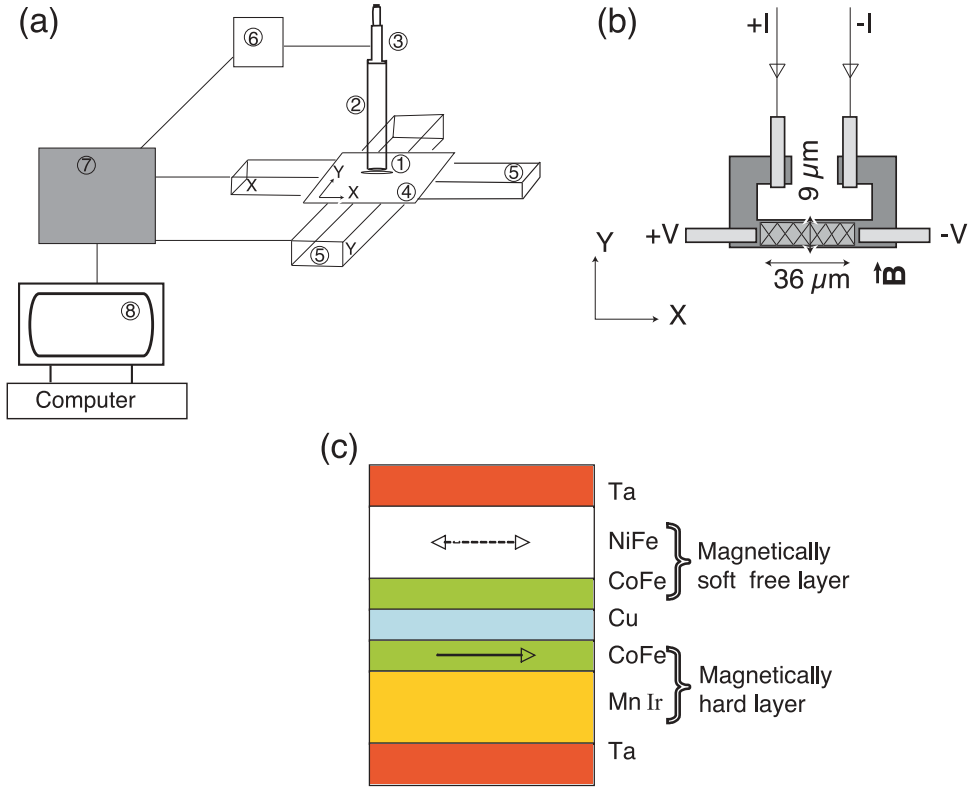

Figure 1. Simplified schematic displaying the main features of the GMR-based scanning magnetometer. (a) Rough sketch illustrating the GMR-based measuring system, with GMR sensor head (see also Figure 1b) (indicated by 1), Plexiglas sample holder (indicated by 2), Micrometric screw controlling the vertical sensor-to-sample distance with a precision of 5 μm (indicated by 3), Plexiglas sample holder stage driven by two DC servomotors allowing horizontal displacements of the sample underneath GMR sensor whose horizontal position is kept fixed (indicated by 4), X-Y DC servomotors move the stage with a positioning precision of 1 μm (indicated by 5), preamplifier (indicated by 6), electronic control unit where output voltage signals of the GMR sensor proportional to the magnetic field are digitized (indicated by 7), and a personal computer through which acquisition of the digitized data and stage motion sequences are controlled (indicated by 8). (b) Close-up view of the yoke-type giant magnetoresistance (GMR) sensor. Hatched area representing the active region with size of the sensing element of 9μm $\times$ 36 μm. A DC current ($\pm$I) biases the sensor, and the voltage output ($\pm$V) is proportional to the resistance of the active region and hence proportional to the magnetic field. (c) A spin valve structure showing a two magnetic layer GMR. The magnetically soft free layer is very sensitive to small fields whereas the magnetically hard layer is insensitive to moderate fields.

component of the magnetic field. This instrument has submillimeter spatial resolution and sensitivity better than 10 nT.

[9] All the above mentioned magnetic imaging devices are sensitive to the vertical component of the magnetic field above the surface of polished samples.

[10] In this paper, in the framework of the efforts of the paleomagnetism and rock magnetism community to map magnetic field at inframillimeter scale, we have developed a new solution: a room temperature scanning magnetic microscope using a giant magnetoresistance (GMR) sensor that maps the horizontal (i.e., in the sample plane) components of the magnetic field above polished samples. It appears to be a powerful and promising instrument for paleomagnetic and rock magnetic investigations as it allows depicting magnetic field above polished samples with a spatial resolution down to about 30 μm.

2. Description of Scanning GMR-Based Microscope

[11] Our current prototype microscope is based on a giant magnetoresistance (GMR) sensor operating at room temperature [*Pannetier-Lecoeur et al.*, 2007]. Figure 1a provides a schematic view of the main features of the GMR-based magnetometer. The

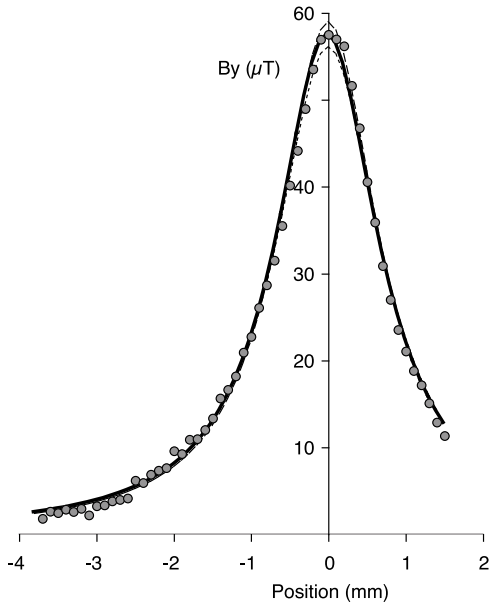

Figure 2. Magnetic field generated by an "infinite" wire carrying a 230 mA static current. Circles represent the data measured with a sensor-to-sample distance set to 800 μm. Solid line is the modeled field at 800 μm, and broken lines are the modeled fields at 780 μm and 820 μm.

sensor, patterned in a 36-μm-long yoke-type shape (Figure 1b), is made of a soft magnetic layer and a hard magnetic layer separated by a copper layer (Figure 1c). The moment of the free layer aligns with the external magnetic field and at zero external magnetic field, it is perpendicular to the magnetic hard layer. The GMR effect resides in a large variation of the electrical resistance in response to an applied field, which rotates the free magnetic layer. To reduce the contact resistance noise, a DC current flows through the GMR sensor and a voltage is measured across the active part (hatched area in Figure 1b) of the sensor. This output voltage signal is directly proportional to the magnetic field along the small width of the sensor. The voltage to magnetic field calibration factor was estimated by placing the sensor at the center of a coil, which was previously calibrated with a gaussmeter.

[12] The GMR sensor is sensitive to the intensity and sign of the component of magnetic field perpendicular to the yoke (Figure 1b). Therefore, scanning the surface of a polished sample with the GMR sensor provides a map of one of the horizontal components of the magnetic field above the sample. The size of the sensing element is 9 μm $\times$ 36 μm. The noise of the GMR sensor is dominated by a low-frequency 1/f noise. The field equivalent noise of the sensors is 10 $nT/\sqrt{Hz}$ at 1Hz and decreases to 0.3 $nT/\sqrt{Hz}$ above 1 kHz for a 1 mA sensing current. The sensor has a bandwidth of 2.5 kHz. During scanning operations, the peak-to-peak noise is about 250 nT. The spatial resolution of the sensor is about 20 μm. This scanning GMR-based magnetometer operates at room temperature and does not require any cooling mechanism. Thus the room temperature sample can be brought into very close proximity down to contact to the sensor. Practically, to avoid damages to the sensor, the minimum sensor-to-sample distance during scanning operation is around 30 μm. The proximity of the sensor to the sample compensates for its rather low field sensitivity. Indeed, the sensor-to-sample distance is a crucial consideration as the magnetic field intensity as well as the spatial resolution decreases with increasing sensor-to-sample distance. However, when scanning with a small sensor-to-sample distance, the magnetic field generated by the 1 mA current flowing into the GMR (2 μT at 100 μm distance, 10 μT at 20 μm distance) may generate an induced magnetization in the sample. This effect is difficult to quantify in details but it is probable that for scanning distances of a few tens of μm the contribution of this induced magnetization will not be negligible. We are currently working on a sensor configuration where we add close (100 nm) to the sensor current line a second current line flowing in the opposite direction to cancel out the magnetic field generated by the sensor.

[13] The instrument is housed in a magnetically shielded room with a residual field <500 nT at CEREGE (Aix-en-Provence). It consists of a GMR sensor mounted on a Plexiglas rod, a Plexiglas sample holder mounted on two DC servomotors, and an electronic control unit (Figure 1a). A computer is used to run measurements and collect data. The sample can be moved horizontally with respect to the fixed sensor along the X and Y directions with a positioning precision of 1 μm, thanks to the two DC servomotors. The distance between sensor and sample is set by moving the sensor vertically down to contact with the sample and subsequently moving it up to the desired height with a micrometric screw with a 5 μm precision. As done by, e.g., *Baudenbacher et al.* [2002], the accuracy of the sensor-to-sample distance was verified by scanning a 150 mm long and 100 μm diameter copper wire carrying a static current of 230 mA with a sensor-to-sample distance set to 800 μm (Figure 2). The comparison of the measured and modeled magnetic fields generated by the current in the wire shows that the scanning distance is accurate to about $\pm$10 μm.

[14] The displacements of the sample below the GMR sensor, whose horizontal position is kept fixed, provide field measurements along one horizontal direction. The output voltage across the active region of the sensor (hatched area in Figure 1b) is proportional to the magnetic field. This voltage signal is amplified in the electronic unit and finally digitized. The GMR sensor can measure field intensities up to ±600 μT. Beyond this maximum field, the sensor response becomes nonlinear with a hysteretic behavior.

[15] In this paper, we report experimental validation measurements of magnetic field distribution of various samples performed with this new GMR scanning device.

3. Measurements and Discussion

3.1. General Features

[16] The current prototype allows scanning one horizontal component of the magnetic field at constant height above polished samples. It offers the possibility to map magnetic field at different distances above the sample by simply increasing the sensor-to-sample distance as well as to map the two horizontal components of the magnetic field (By and Bx) by simply rotating the sample holder by 90° without having to lift the sensor so that the sensor-to-sample distance remains unchanged. The error in the rotation angle of the stage is negligible (<1°). However, there is fairly large inherent imprecision when repositioning the sample after rotation because in the general case the sample is not perfectly centered on the stage. Therefore the superimposition between the two magnetic maps is not a trivial exercise. This problem will be overcome in the future by measuring simultaneously the two horizontal components of the magnetic field by using two perpendicular sensors with a known spatial offset. Measuring the two horizontal components is crucial for the inversion of magnetic field data acquired with the GMR-based scanning system in order to access to magnetization sources distribution, namely the intensities and directions of the magnetized areas within the sample. Indeed, the third component of the magnetic field (the vertical component) can be calculated from the two horizontal components [*Lima and Weiss*, 2009]. Also the measurements at various sensor-to-sample distances will make data inversion more robust (see, e.g., *Quesnel et al.* [2007, 2008] for a similar discussion regarding the inversion of satellite data).

[17] In the following, we report magnetic field measurements of samples associated with natural remanent magnetization (NRM) and saturation remanent magnetization (sIRM) in order to exemplify the detection capabilities and the high resolution of this prototype GMR-based microscope.

3.2. Test Using a Natural Sample With a Simple Geometry

[18] We first test our prototype with a relatively simple sample. We used a 450-μm-diameter melted micrometeorite (Figure 3a) sampled in Antarctica [*Rochette et al.*, 2008]. The choice of this particular sample was dictated by the need to have a simple shape, to ease the comparison of true measurements to predicted ones. This micrometeorite was saturated with a 1 T magnetic field and has a magnetic moment of 2.60×10^{-7} Am^2 as measured independently with a 2G SQUID magnetometer. We provide magnetic measurements performed at sensor-to-sample distance at 600 μm with a step size of 70, 80 and 75 μm (Figures 3c–3e), as well as corresponding modeled magnetic maps (Figures 3f–3h). These three sets of magnetic maps correspond to the same sample saturated along three orthogonal directions. In Figure 3c, the sample is saturated along the scanning and measuring direction (y axis). The dipolar structure of the source is clearly visible with the maximum field located above the sample, with weaker opposite sign lobes on the top and bottom sides. Figure 3d displays the magnetic map when the sample is saturated in plane (x axis) but perpendicular to the scanning and measuring direction. This map exhibits the expected four-lobe structure with equal absolute negative and positive extrema. Finally, Figure 3e exemplifies the case when the sample is saturated along the vertical axis, with two opposite sign lobes, the negative located at the top and the positive at the bottom of the sample.

[19] For the modeled maps, we used a forward approach for a sample with a simple geometry (a 450-μm-diameter sphere) and with a known magnetic moment (2.60×10^{-7} Am^2). The forward code is based on an equivalent source dipole (EDS) approach [*Langlais and Purucker*, 2007], which was modified to take into account the planar assumption. The choice of the ESD formalism was made because this is the method that we will apply later to solve the inverse problem between magnetic measurements and magnetization distribution of more complex samples. The predicted field is very similar both in shape and intensity to the measured field. For the case with saturation along y axis, the

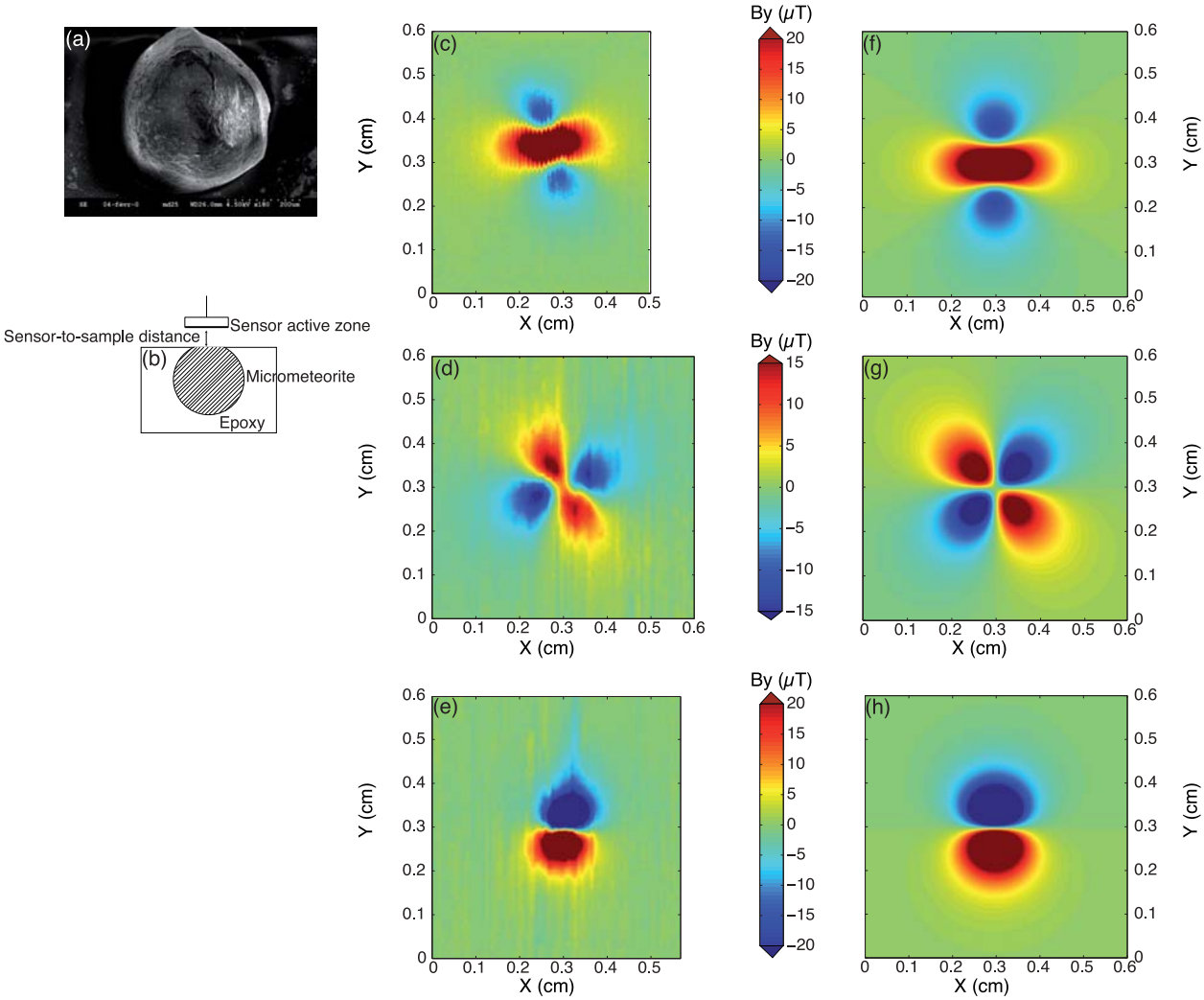

Figure 3. Maps of the magnetic field generated by a 450-μm-diameter cosmic spherule from Antarctica. (a) SEM image of this micrometeorite that had been exposed afterward to 1 T saturating magnetic field (sIRM). (b) Experimental setup illustrating magnetic field data acquisition method above a polished sample. (c–e) Experimental results for the By component measured at 600 μm distance above the same sample saturated along three different orthogonal directions (Y, X, and Z). The scanning step is 70, 80, and 75 μm. (f–h) Forward modeled field maps of the By components, using the equivalent dipole source approach (EDS). Simulated maps shown in Figures 3f–3h correspond with experimental maps in Figures 3c–3e. Note that color scales are modified in order to enhance dynamic contrast of images. Triangles pointing upward and downward stand for saturation of the scale.

measured extrema are −14.6/+74.7 μT, while these are predicted to be −17.5/+83.5 μT. Predictions for saturation along *x* axis are equally satisfactory, with measured and predicted extrema equal to −17.0/+18.2 and ±23.6 μT, respectively. This consistency also holds for the sample saturated along Z axis with values of −70.1/+65.1 and ±72.4 μT for the measurements and the predictions, respectively. The overall similarity of the measurements to the predictions suggests that the measurements are reliable and accurate. The good estimate of the field extrema values confirms that the sensor-to-sample distance is accurate. There are however noticeable geometrical dissimilarities between measured and modeled maps. The most striking dissimilarity is the rotation between the experimental and modeled maps (Figures 3c and 3f, for instance) as well as "distortion" of the experimental maps (Figure 3c, for instance). First, this is due to the micrometeorite that is not a perfect sphere (Figure 3a). Second, there is a probable slight relative misalignment between the sensor and the magnetization direction of the sample whereas in the modeled maps the magnetization is taken exactly toward the Y and X directions. The

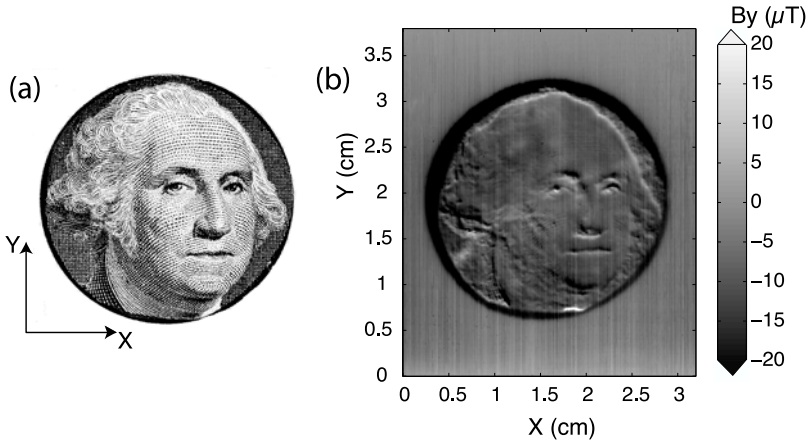

Figure 4. Magnetic image of George Washington's face in a dollar bill saturated at 1 T along the vertical (out-of-page) direction. (a) Picture of the sample. (b) Magnetic field map of the horizontal component By as measured at 60 μm above the bill. Scanning step is 50 μm along the x axis and 30 μm along the y axis. Triangles pointing upward and downward stand for saturation of the scale.

apparent rotation and distortion of the measured maps can therefore be accounted for the combination of the modeled By and Bx maps (Figures 3f and 3g): $By_{measured} = By_{modelled} \cos\alpha + Bx_{modelled} \sin\alpha$, where α is the misalignment angle.

3.3. Illustration of the Spatial Resolution of the GMR Scanner

[20] Illustrations of the high spatial resolution of our prototype are provided in Figures 4 and 5. Several authors have already realized magnetic scans of a one-dollar bill (whose ink contains ferromagnetic particles) in order to check for the resolution of their instruments [*Howells et al.*, 1997; *Uehara and Nakamura*, 2007; *Kletetschka*, and Adachi, 2008; *Uehara and Nakamura*, 2008]. Figure 4 is a magnetic map obtained with the GMR scanner with a sensor-to-sample distance of 60 μm. This portion of the bill was magnetized by a downward 1 T magnetic field and had a bulk sample magnetic moment of 3.68×10^{-6} Am^2 as measured with a 2G SQUID magnetometer. Our image shows details of the facial expression that are about 150 μm in size.

[21] Figure 5 displays a line scan as measured 40 μm above a hemo-ilmenite ore sample from Allard Lake, Quebec [*Hargraves*, 1959; *McEnroe et al.*, 2007] with a step size of 4 μm. This sample consists of ilmenite host grains (darker) with large hematite exsolution lamellae (lighter) parallel to (0001) and with second and subsequent generations of hematite lamellae also parallel to (0001). Large 1st generation hematite lamellae are 40–50 μm thick. Within these hematite lamellae are finer ilmenite exsolution from a few microns to few nanometers in thickness [*McEnroe et al.*, 2007]. The natural remanent magnetization of this ore sample is 95 A/m, is in plane, and pointing to the bottom of the picture. This is a favorable case where the negative anomalies are centered above the magnetic sources (see Figure 3c). The line scan shows a very detailed correspondence with the hematite lamellae (Figure 5). Features that are only a few tens of μm are easily resolvable.

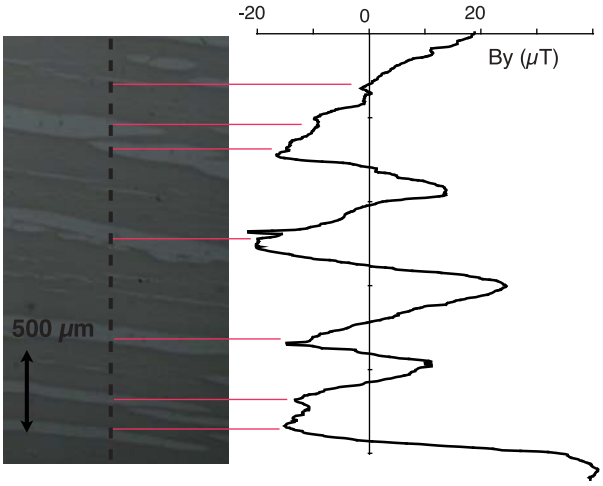

Figure 5. Line scan measured 40 μm above a polished hemo-ilmenite ore sample from Lac Ellen, Quebec. The step size is 4 μm. The natural remanent magnetization of the sample is in plane, pointing toward the bottom of the page. The lighter bands on the reflected light image are large hematite lamellae with abundant small ilmenite lamellae within the hematite. The host ilmenite is darker. The negative magnetic peaks correspond to the magnetized hematite lamellae.

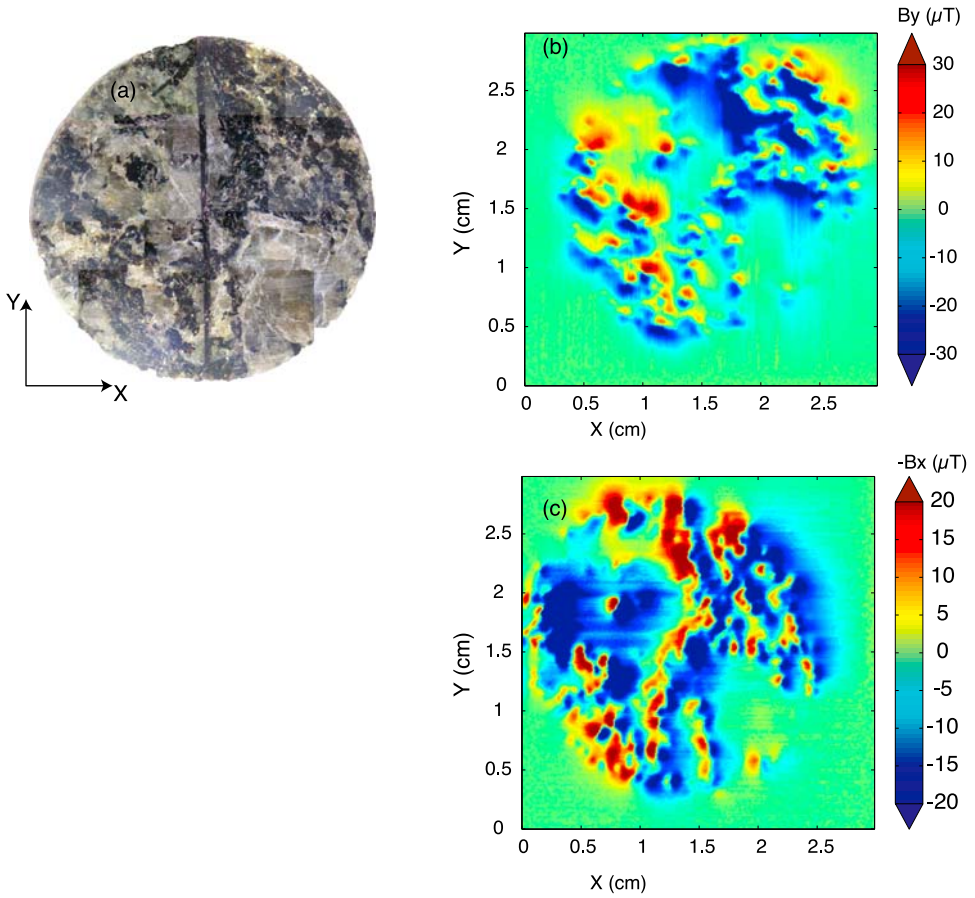

Figure 6. Magnetic maps of the field generated by a 1-mm-thick slice of a norite from Norway. Shown are the two horizontal components (By and −Bx) of the natural remanent magnetization (NRM) field as measured 400 μm above the surface of the sample. (a) An optical image of the 1-mm-thick slice of norite showing the ground mass that contains pyroxene and magnetite (dark areas) and plagioclase feldspar (whitish and greyish zones). Black arrow indicates the scanning direction. (b) Magnetic map of the By component of the NRM field. (c) Scan of the −Bx component of the NRM field. Scanning step in Figures 6b and 6c is 150 μm. Color scales follow the same convention as in Figure 3. Note the good agreement with the optical image in Figure 6a since the most visible nonmagnetic areas of the scans (bottom right corner of both Figures 6b and 6c) correspond to the whitish and greyish zones identified in Figure 6a.

3.4. Natural Remanent Magnetization Imaging

[22] We have scanned a norite sample from the Proterozoic Bjerkreim-Sokndal intrusion in Norway [*McEnroe et al.*, 2004a, 2004b]. This rock carries a strong natural remanent magnetization of 55 A/m (1.7×10^{-2} Am^2 kg^{-1}). We performed magnetic scans on a representative sample (Figure 6a). Figures 6b and 6c represent magnetic maps of the NRM By and Bx field components, respectively, as measured 400 μm above the polished 1-mm-thick slice of the norite. These magnetic images exhibit numerous submillimeter-sized magnetic anomalies within the sample. These correspond to the spatially heterogeneous distribution of the magnetization within the sample. The patchy pattern in the sample is fairly consistent with the optical image (Figure 6a). Indeed, the whitish and greyish area observed on the optical image highlighting the presence of nonmagnetic minerals match the zero-field zones of the magnetic images (Figures 6b and 6c).

4. Conclusion

[23] We demonstrated the ability of this new room temperature GMR magnetic scanner to detect and map the horizontal components of magnetization of polished rock samples with a high spatial resolution (down to a few tens of μm, the main limitation being the scanning distance). It is a simple and rugged device alternative to the more complex low-Tc SQUID microscope. Although some other

experiments (such as the low-Tc SQUID microscope running at the Massachusetts Institute of Technology) have been shown to be much more sensitive, our prototype compensates for its moderate sensitivity by a high spatial resolution with a sensor-to-sample distance that can be as low as 30 μm during scanning operation, making it a valuable instrument for detailed rock magnetic studies (small-scale identification of magnetic carriers in particular).

[24] This instrument is sensitive to the horizontal components of the magnetic field. Inversion of the data can be made by using two perpendicular horizontal components to compute the vertical one. Data acquisition at different sensor-to-sample distances also helps constraining inversion.

[25] Following these first promising measurements, further improvements are envisaged:

[26] 1. The width of the sensor will be reduced from 36 μm to 5 μm in order to increase further its spatial resolution while keeping the same sensitivity.

[27] 2. The ambient residual magnetic field in the shielding room amounts to <500 nT. Although this has no significant effect on samples that have been imparted a sIRM, we will reduce this residual field with additional magnetic shields.

[28] 3. A new generation of the device will eliminate the noise linked to the electronic unit by using a gradiometer geometry.

[29] 4. We will also perform simultaneous measurements of X and Y axes.

Acknowledgments

[30] This study was supported by Agence Nationale de la Recherche (project ANR-05-JCJC-0133). The authors thank G. Legoff and G. Cannies from the CEA (Saclay) who worked on the mechanics of the GMR-based device. F. Hankard would like to thank P. Dussouillez and E. Lima for useful advice.

References

Baudenbacher, F., N. T. Peters, and J. P. Wikswo (2002), High resolution low-temperature superconducting quantum interference device microscope for imaging magnetic fields of samples at room temperatures, *Rev. Sci. Instrum.*, *73*, 1247–1254, doi:10.1063/1.1448142.

Baudenbacher, F., L. E. Fong, J. R. Holzer, and M. Radparvar (2003), Monolithic low-transition-temperature superconducting magnetometers for high resolution imaging magnetic fields of room temperature samples, *Appl. Phys. Lett.*, *82*, 3487–3489, doi:10.1063/1.1572968.

Egli, R., and F. Heller (2000), High-resolution imaging using a high-Tc superconducting quantum interference device (SQUID) magnetometer, *J. Geophys. Res.*, *105*, 25,709–25,727, doi:10.1029/2000JB900192.

Fong, L. E., J. R. Holzer, K. K. McBride, E. A. Lima, and F. Baudenbacher (2005), High-resolution room-temperature sample scanning superconducting quantum interference device microscope configurable for geological and biomagnetic applications, *Rev. Sci. Instrum.*, *76*, 053703, doi:10.1063/1.1884025.

Gattacceca, J., M. Boustie, B. P. Weiss, P. Rochette, E. A. Lima, L. E. Fong, and F. J. Baudenbacher (2006), Investigating impact demagnetization through laser impacts and SQUID microscope, *Geology*, *34*, 333–336, doi:10.1130/G21898.1.

Hargraves, R. (1959), Magnetic anisotropy and remanent magnetization in hemo-ilmenite from ore deposits of Allard Lake, Quebec, *J. Geophys. Res.*, *64*, 1565–1573, doi:10.1029/JZ064i010p01565.

Howells, G., R. J. Prance, T. D. Clark, and H. Prance (1997), Detection of printed magnetic inks using a room-temperature scanning magnetic microscope, *Meas. Sci. Technol.*, *8*, 734–737, doi:10.1088/0957-0233/8/7/007.

Kletetschka, G., and T. Adachi (2008), Magnetic detection of large magnetic fields that occurred during the Vredefort impact, implications for Mars magnetic anomalies, paper presented at Large Meteorite Impacts and Planetary Evolution IV, Lunar and Planet. Inst., Vredefort Dome, South Africa.

Langlais, B., and M. Purucker (2007), A polar magnetic paleopole associated with Apoolinaris Patera Mars, *Planet. Space Sci.*, *55*, 270–279, doi:10.1016/j.pss.2006.03.008.

Lima, E. A., and B. P. Weiss (2009), Obtaining vector magnetic field maps from single-component measurements of geological samples, *J. Geophys. Res.*, *114*, B06102, doi:10.1029/2008JB006006.

McEnroe, S. A., J. R. Skilbrei, P. Robinson, F. Heidelbach, F. Langenhorst, and L. L. Brown (2004a), Magnetic anomalies, layered intrusions and Mars, *Geophys. Res. Lett.*, *31*, L19601, doi:10.1029/2004GL020640.

McEnroe, S. A., L. L. Brown, and P. Robinson (2004b), Earth analog for Martian magnetic anomalies: Remanence properties of hemo-ilmenite norites in the Bjerkreim-Sokndal Intrusion, Rogaland, Norway, *J. Appl. Geophys.*, *56*(3), 195–212.

McEnroe, S. A., P. Robinson, F. Langenhorst, C. Frandsen, M. P. Terry, and T. Boffa Ballaran (2007), Magnetization of exsolution intergrowths of hematite and ilmenite: Mineral chemistry, phase relations, and magnetic properties of hemo-ilmenite ores with micron- to nanometer-scale lamellae from Allard Lake, Quebec, *J. Geophys. Res.*, *112*, B10103, doi:10.1029/2007JB004973.

Nowaczyk, N. R., H.-U. Worm, A. Knecht, and J. H. Hinken (1998), Imaging distribution patterns of magnetic minerals by a novel high-Tc-SQUID-based field distribution measuring system: Applications to Permian sediments, *Geophys. J. Int.*, *132*, 721–726, doi:10.1046/j.1365-246X.1998.00496.x.

Pannetier-Lecoeur, M., et al. (2007), Low noise magnetoresistive sensors for current measurement and compasses, *J. Magn. Magn. Mater.*, *316*(2), E246–E248.

Quesnel, Y., B. Langlais, and C. Sotin (2007), Local inversion of magnetic anomalies: Implication for Mars' crustal evolution, *Planet. Space Sci.*, *55*(3), 258–269, doi:10.1016/j.pss.2006.02.004.

Quesnel, Y., B. Langlais, C. Sotin, and A. Galdéano (2008), Modeling and inversion of local magnetic anomalies, *J. Geophys. Eng.*, *5*, 387–400, doi:10.1088/1742-2132/5/4/003.

Rochette, P., L. Folco, C. Suavet, M. van Ginneken, J. Gattacceca, N. Perchiazzi, R. Braucher, and R. P. Harvey (2008), Micrometeorites from the Transantarctic Mountains,

Proc. Natl. Acad. Sci. U. S. A., *105*, 18,206–18,211, doi:10.1073/pnas.0806049105.

Thomas, I. M., T. C. Moyer, and J. P. Wikswo Jr. (1992), High resolution magnetic susceptibility imaging of geological thin sections: Pilot study of a pyroclastic sample from the Bishop Tuff, California, U.S.A., *Geophys. Res. Lett.*, *19*, 2139–2142, doi:10.1029/92GL02322.

Uehara, M., and N. Nakamura (2007), Scanning magnetic microscope system utilizing a magneto-impedance sensor for a nondestructive diagnostic tool of geological samples, *Rev. Sci. Instrum.*, *78*, 043708, doi:10.1063/1.2722402.

Uehara, M., and N. Nakamura (2008), Identification of stable remanence carriers through a magneto-impedance scanning magnetic microscope, *Stud. Geophys. Geod.*, *52*, 211–223, doi:10.1007/s11200-008-0014-2.

Wang, H. W., X. Y. Kong, Y. F. Ren, H. W. Yu, H. S. Ding, S. P. Zhao, G. H. Chen, L. H. Zhang, Y. L. Zhou, and Q. S. Yang (2003), Magnetic microscopy based on high-Tc SQUIDs for room temperature samples, *Supercond. Sci. Technol.*, *16*, 1310–1313, doi:10.1088/0953-2048/16/11/010.

Weiss, B. P., J. L. Kirschvink, F. J. Baudenbacher, H. Vali, N. T. Peters, F. A. Macdonald, and J. P. Wikswo (2000), A low temperature transfer of ALH84001 from Mars to Earth, *Science*, *290*, 791–795, doi:10.1126/science.290.5492.791.

Weiss, B. P., E. A. Lima, L. E. Fong, and F. J. Baudenbacher (2007a), Paleointensity of the Earth's magnetic field using SQUID microscopy, *Earth Planet. Sci. Lett.*, *264*, 61–71, doi:10.1016/j.epsl.2007.08.038.

Weiss, B. P., E. A. Lima, L. E. Fong, and F. J. Baudenbacher (2007b), Paleomagnetic analysis using SQUID microscopy, *J. Geophys. Res.*, *112*, B09105, doi:10.1029/2007JB004940.

Weiss, B. P., L. E. Fong, H. Vali, E. A. Lima, and F. J. Baudenbacher (2008), Paleointensity of the ancient Martian magnetic field, *Geophys. Res. Lett.*, *35*, L23207, doi:10.1029/2008GL035585.